machines

MDPI

Article

DBO-Optimized Fuzzy PID Control for Position Tracking of a Pilot-Operated Proportional Directional Valve with Dead-Zone Nonlinearity

Hui Guo, Boqiang Shi *, Hu Chen, Haoran Zhu and Bingbing Liu

School of Mechanical Engineering, University of Science and Technology Beijing, Beijing 100083, China; d202410315@xs.ustb.edu.cn (H.G.)
* Correspondence: shiboqiang@ustb.edu.cn

Abstract

This study addresses the high-precision position control problem of pilot-operated proportional directional valves under dead-zone nonlinearity. A fuzzy PID-based position control strategy optimized by the dung beetle optimizer (DBO-FPID) is proposed to alleviate switching lag and accuracy degradation caused by dead-zone effects. First, a refined nonlinear model combining theoretical analysis and AMESim simulation is established to quantitatively characterize the dead-zone evolution mechanism of the valve system, and the dead-zone range of the directional valve is identified as ±34.5% of the duty cycle. On this basis, a multiphysics co-simulation model is developed to analyze the static and dynamic characteristics of the pilot valve and the main spool. Then, the DBO algorithm is introduced to optimize the key parameters of the fuzzy PID controller by minimizing an objective function based on the integral of time-weighted absolute error (ITAE), thereby improving the controller's compensation capability for dead-zone nonlinearity. Simulation results show that, compared with DBO-PID, the proposed DBO-FPID control strategy reduces the rise time by 54.4%. During triangular and sinusoidal position tracking, the dead-zone residence time is reduced by 47.5% and 44.8%, respectively, while the mean absolute error remains below 0.2 mm. Experiments further validate the effectiveness of the proposed control strategy for high-precision position control of the pilot-operated proportional directional valve.

Keywords: pilot-operated proportional directional valve; position tracking; fuzzy PID control; dung beetle optimizer; dead-zone nonlinearity; electro-hydraulic control

Check for updates

Academic Editor: Carmine Maria Pappalardo

Received: 7 April 2026
Revised: 30 April 2026
Accepted: 2 May 2026
Published: 5 May 2026

Copyright: © 2026 by the authors. Licensee MDPI, Basel, Switzerland. This article is an open access article distributed under the terms and conditions of the Creative Commons Attribution (CC BY) license.

1. Introduction

Pilot-operated proportional directional valves are widely employed in hydraulic systems of construction machinery, agricultural equipment, and other high-power industrial applications, where they act as a key interface between electronic control units and hydraulic actuators [1,2]. As a critical control component in large-scale hydraulic equipment, their dynamic response and position control accuracy have a direct impact on motion quality, operating efficiency, and overall system stability [3]. With the increasing demand for high-precision positioning and rapid dynamic response in modern industry, enhancing the control performance of proportional valves under nonlinear effects has become a major research focus [4]. In particular, dead-zone nonlinearity, hysteresis, and pilot–main stage coupling can markedly deteriorate tracking accuracy and transient response, which poses

significant challenges for high-performance position control of pilot-operated proportional directional valves [5].

However, in the structural design of pilot-operated proportional valves, positive overlap is commonly introduced in the pilot stage to reduce internal leakage and improve volumetric efficiency. While this design enhances sealing performance, it inevitably leads to significant dead-zone nonlinearity [6]. Furthermore, owing to the combined effects of spring preload, hydraulic force coupling, and cascade transmission between the pilot and main stages, the valve system may exhibit switching delay and asymmetric dynamic response near the neutral position [7]. These nonlinear effects directly degrade spool position tracking performance, especially under small-signal operating conditions and during reversing processes [8]. Previous studies [9] have addressed cascade dead zones, micro-flow regions, and dead-zone detection and compensation, suggesting that dead-zone nonlinearity is one of the major bottlenecks restricting further improvement in the control performance of pilot-operated proportional valves.

Meanwhile, studies on electro-hydraulic system dynamics have shown that the dynamic behavior of pilot-operated proportional directional valves is influenced not only by valve flow characteristics and control inputs but also by the combined effects of mechanical vibration, pressure pulsation, and spool-pair interaction. Existing studies have indicated that, when the nonlinear characteristics of hydraulic valves are considered, external mechanical vibration may change the amplitude and spectral characteristics of pressure pulsations in the system, thereby further affecting spool stability, control accuracy, and the dynamic response near the dead zone [10]. These findings suggest that vibration-induced pressure fluctuations may be an important factor influencing the dynamic performance of proportional valves. In addition, modeling and experimental studies on spool-pair interaction in hydraulic directional valves have shown that the coupled behavior of the valve body–spool pair is jointly determined by the relative motion between the valve body and the spool, frictional conditions, and external vibration excitation [11]. For the pilot-operated proportional directional valve investigated in this study, the dynamic coupling between the pilot stage and the main stage is reflected not only in the cascaded transmission of pressure and flow, but may also be affected by spool-pair contact/friction characteristics and the propagation of pressure fluctuations. Therefore, interpreting the pilot stage–main stage coupling phenomenon from the broader perspective of electro-hydraulic system dynamics helps strengthen the physical basis for the control problem addressed in this paper.

To address the nonlinear challenges in pilot-operated proportional valves, such as dead zone, hysteresis, and parameter variations, a variety of control strategies have been proposed. Conventional PID control is still widely used in electro-hydraulic systems because of its simple structure, ease of implementation, and high engineering reliability [12]. In addition, several improved PID schemes [13], such as gain-adjusted and variable-integral PID methods [14,15], have been developed to enhance transient response and system stability. However, under operating conditions with pronounced dead-zone nonlinearity and complex disturbances, fixed-parameter or locally modified PID controllers still struggle to simultaneously achieve fast response, low overshoot, and high steady-state accuracy [16]. In contrast, fuzzy PID control can adjust controller parameters online based on expert rules, thereby improving the adaptability of the system to nonlinearities, uncertainties, and parameter perturbations [17,18]. As a result, it has been successfully applied to a variety of electro-hydraulic servo systems and has demonstrated promising control performance [19,20]. Nevertheless, the effectiveness of a fuzzy PID controller largely depends on the proper selection of scaling factors, quantization factors, and initial PID gains. Since these parameters are usually strongly coupled, their optimization space is often multimodal, nonlinear, and even discontinuous. Consequently, manual tuning is

not only time-consuming but also highly subjective [21,22]. In recent years, metaheuristic algorithms such as genetic algorithms (GA) [23,24] and particle swarm optimization (PSO) [25,26] have been increasingly introduced into controller parameter optimization, providing new approaches for tuning fuzzy PID controllers. However, when dealing with complex objective functions caused by valve dead-zone effects, these algorithms may still suffer from slow convergence, premature convergence, and a tendency to become trapped in local optima [27]. Therefore, for controller parameter optimization of pilot-operated proportional valves under dead-zone nonlinearity, it remains necessary to explore more efficient and robust intelligent optimization methods.

To overcome the above limitations, this study investigates the dead-zone characteristics of the pilot valve in detail and, on this basis, proposes a fuzzy PID-based position control method for the dead-zone problem of pilot-operated proportional directional valves, with the controller parameters optimized by the dung beetle optimizer (DBO). The fuzzy PID scheme is adopted because it can adjust the control parameters online according to the error and its rate of change, making it more suitable than fixed-gain PID for handling nonlinearities such as dead zone, hysteresis, and parameter variations in pilot-operated proportional directional valves [28]. However, the control performance of fuzzy PID depends strongly on the proper configuration of its key parameters. Therefore, DBO is further introduced to optimize these parameters. Inspired by the ball-rolling, orientation, foraging, and stealing behaviors of dung beetles, DBO exhibits a good balance between global exploration and local exploitation and is well-suited for solving strongly nonlinear and multimodal engineering optimization problems [29,30]. To improve the controller's compensation capability for dead-zone nonlinearity, an objective function based on the integral of time-weighted absolute error (ITAE) is constructed, on the basis of which the fuzzy PID parameters are optimized. Finally, the proposed method is validated through simulations and experiments and compared with conventional PID and standard fuzzy PID controllers to evaluate its improvements in response speed, steady-state accuracy, and dead-zone compensation performance.

The remainder of this paper is organized as follows. Section 2 presents the working principle and mathematical model of the pilot-operated proportional directional valve, with particular emphasis on the formation mechanism of dead-zone nonlinearity. Section 3 develops a multiphysics simulation model and analyzes the static and dynamic characteristics of the pilot valve and the main valve. Section 4 details the design of the DBO-fuzzy PID controller and demonstrates its effectiveness through simulations under different tracking trajectories. Section 5 describes the experimental setup and validates the proposed control strategy on a physical test platform. Finally, Section 6 concludes the paper.

2. Working Principle and Mathematical Modeling of the Pilot-Operated Proportional Directional Valve

2.1. Structure and Operating Principle

The pilot-operated proportional directional valve investigated in this study is a directional control unit in a load-sensing multi-way valve. It mainly consists of a pilot proportional spool valve, a main valve, a pressure compensator, and an onboard controller. The overall structure is shown in Figure 1. The pilot valve is a positively overlapped 4/3 proportional spool valve that directly controls the motion of the main spool. The main valve spool has a typical multi-way valve configuration, and its metering edges are designed with specially shaped throttling grooves to improve the flow regulation characteristics. In addition, two return springs are installed at both ends of the spool to ensure that it can reliably return to the neutral position in the absence of a control signal. The

pressure compensator is an independent component located between the inlet port and the main spool. During the operation of the multi-way valve, it maintains a constant pressure drop across the main spool, thereby ensuring that the flow characteristics are unaffected by variations in load pressure. The onboard PCB integrates the position sensing circuit, solenoid driving circuit, and feedback controller to achieve closed-loop position control of the directional valve.

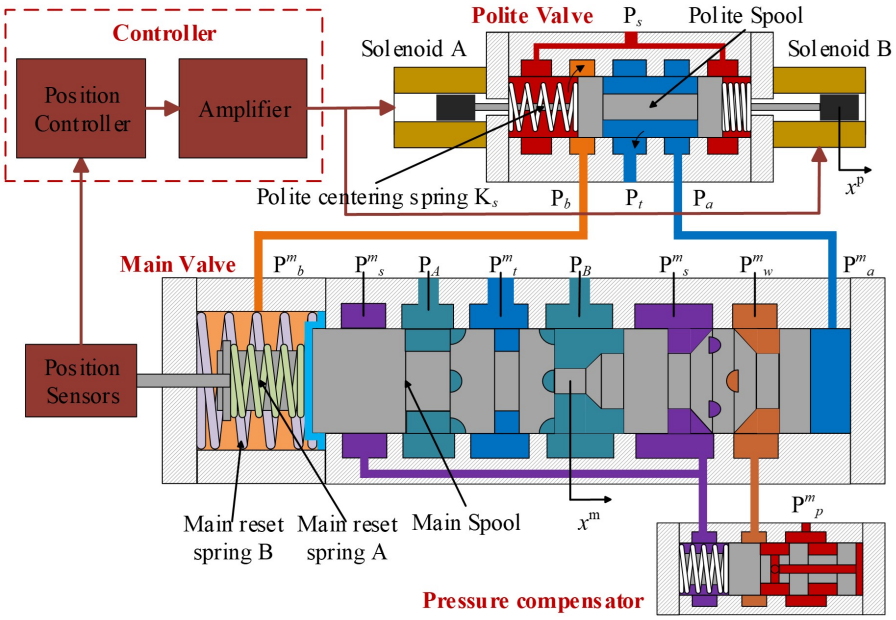


Figure 1. Structural schematic of a pilot-operated proportional directional valve.

As shown in Figure 2, the directional valve has four operating states. In Figure 2a, the main spool is in the neutral position. At this stage, either the pilot valve is not energized, or the input current is below the dead-zone threshold. Consequently, the left and right control chambers of the main spool are both connected to the return port of the pilot valve, resulting in equal pressure in the two chambers. Under the action of the return springs, the main spool remains in the neutral position.

In Figure 2b, the main spool is in the lift position. In this state, high-pressure oil is supplied to working port B. When solenoid B of the pilot valve is energized, and the input current exceeds the dead-zone threshold, the supply port P_s of the pilot valve is connected to port P_b, while port P_a is connected to the tank port P_t. As a result, hydraulic oil flows into the left control chamber of the main spool, increasing the chamber pressure and driving the spool rightward. Accordingly, port P_s^m of the main valve is connected to port P_A, while port P_B is connected to the tank port P_t^m.

Figure 2c shows the main spool in the lower position. In this state, high-pressure oil is supplied to working port A. When the input current applied to solenoid A of the pilot valve exceeds the dead-zone threshold, the supply port P_s is connected to port P_a, while port P_b is connected to the tank port P_t. Hydraulic oil then flows into the right control chamber of the main spool, increasing the chamber pressure and driving the main spool leftward. Consequently, port P_s^m of the main valve is connected to port P_B, while port P_A is connected to the tank port P_t^m.

In Figure 2d, the valve is in the float position. At this stage, the main spool moves to its leftmost position, and ports P_A and P_B are both connected to the tank port P_t^m.

The onboard PCB performs feedback control based on the displacement signal measured by the main spool position sensor and generates a control voltage for the pilot valve. By regulating the pilot supply circuit, it thereby controls the position of the main spool.

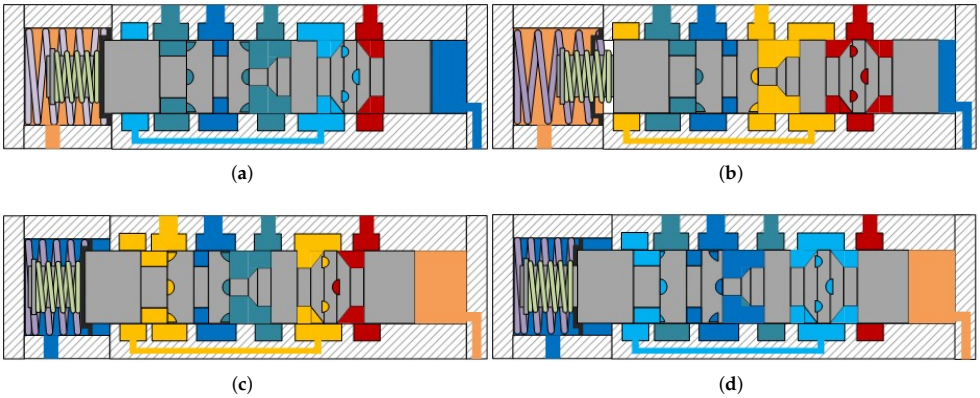


Figure 2. Operating states of the pilot-operated proportional directional valve. (**a**) Neutral position. (**b**) Lift position. (**c**) Lower position. (**d**) Float position.

2.2. Mathematical Model

The proportional solenoid acts as an electromechanical actuator that converts electrical input into electromagnetic force to drive spool motion. Each solenoid is driven by a PWM-controlled single-transistor circuit. The duty cycle, denoted by τ_k, determines the average voltage applied to the solenoid coil, thereby affecting the coil current and the resulting electromagnetic force. This relationship can be expressed as follows:

$$u_k = \frac{\bar{u}}{R_k}\tau_k, k = a, b \tag{1}$$

where $\bar{u}$ denotes the supply voltage, and R_k denotes the coil resistance. When the voltage u_k is applied to the solenoid, the coil current i_k evolves according to the electromagnetic dynamics. Defining the current difference as $i_\Delta = i_a - i_b$ and the voltage difference as $u_\Delta = u_a - u_b$, the corresponding dynamic relationship between u_Δ and i_Δ can be expressed as

$$u_\Delta = R_\Delta i_\Delta + L_\Delta \frac{di_\Delta}{dt} \tag{2}$$

where $R_\Delta = R_a = R_b$ denotes the resistance of each solenoid coil, and $L_\Delta = L_a = L_b$ represents the inductance of each solenoid coil.

Under the action of the electromagnetic force, the pilot spool moves by overcoming the spring force, hydraulic force, and viscous damping force, as shown in Figure 3. The focus of this study is the influence of dead-zone nonlinearity on the dynamic response. Within the considered operating range, the dynamic equation can be simplified as follows:

$$m\frac{\mathrm{d}^2x}{\mathrm{dt}^2} = F_{m,\Delta} - b\frac{\mathrm{d}x}{\mathrm{dt}} - 2k_s x - F_{\mathrm{jet}} \tag{3}$$

where m and x denote the mass and displacement of the pilot spool, respectively. $F_{m,\Delta}$ denotes the electromagnetic force difference, b is the viscous damping coefficient, k_s is the spring stiffness, and F_{jet} denotes the hydraulic flow force acting on the spool , and its detailed expression can be found in [31].

The orifice flow rate of the pilot valve can be expressed as

$$Q_k = \alpha_{sk}A_{sk}(x)\sqrt[s]{\Delta p_{sk}} + \alpha_{tk}A_{tk}(x)\sqrt[s]{\Delta p_{tk}}, j = s, t \tag{4}$$

where $\alpha_{jk} = C_{jk}\sqrt{2/\rho}$, and $\sqrt[s]{\cdot} = \sqrt{|\cdot|}\,\mathrm{sign}(\cdot)$ denotes the signed square-root function. C_{jk} is the flow coefficient for each valve port, and ρ denotes the hydraulic fluid density. $A_{jk}(x)$ denotes the flow area between ports j and k, which is a function of the spool displacement x. $\Delta p_{jk} = p_j - p_k$ denotes the pressure difference between ports j and k. The

orifices of the pilot valve are circular. The relationship between the flow area function $A_{jk}(x)$ and the spool displacement x is shown in Figure 4. The corresponding analytical expression can be approximated as

$$A_{jk}(x) \approx k_{1,jk}x + k_{2,jk}x^2 \tag{5}$$

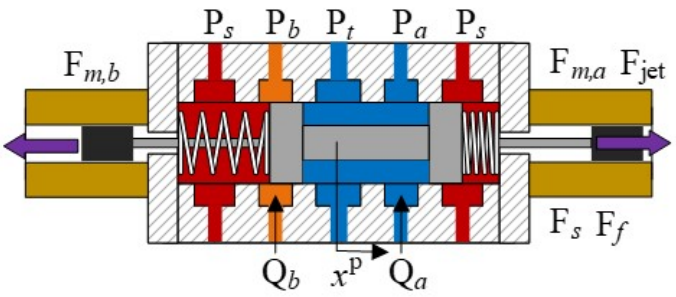


Figure 3. Schematic of the forces acting on the pilot spool.

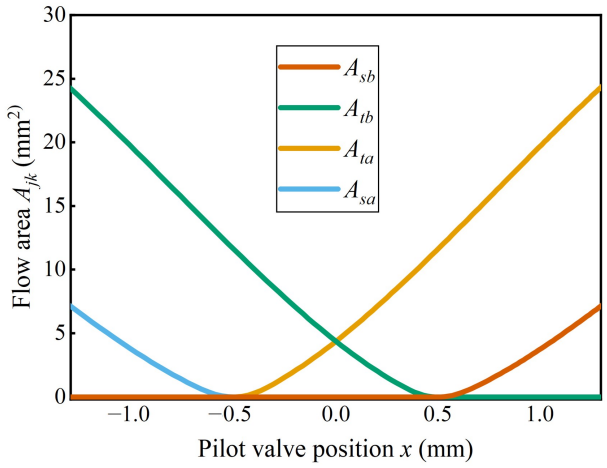


Figure 4. Flow rate curves of the pilot valve.

It can be observed that when $x \in [-0.5\text{ mm}, 0.5\text{ mm}]$, the flow areas of working ports a and b are both zero. In this condition, the control chambers at both ends of the main spool are connected to the tank, resulting in equal pressures in the two chambers. Consequently, the main spool remains at the neutral closed position. This region causes the directional valve to exhibit no response to small input signals, leading to a hysteresis effect commonly referred to as the dead zone.

The pressure-flow equations for the control chambers on either side of the main spool are as follows:

$$\begin{cases} \frac{\mathrm{d}}{\mathrm{d}t}P_a^m = \frac{\beta}{V_a^m(x^m)}\left(-Q_a + A_a^m\frac{\mathrm{d}x^m}{\mathrm{d}t}\right) \\ \frac{\mathrm{d}}{\mathrm{d}t}P_b^m = \frac{\beta}{V_b^m(x^m)}\left(Q_b - A_b^m\frac{\mathrm{d}x^m}{\mathrm{d}t}\right) \end{cases} \tag{6}$$

where $V_a^m(x^m) = V_{a0}^m - A^m x^m$ and $V_b^m(x^m) = V_{b0}^m + A^m x^m$ denote the volumes of the left and right control chambers, respectively. V_{a0}^m and V_{b0}^m denote the initial volumes of the left and right control chambers, respectively. β is the bulk modulus of the hydraulic fluid, x^m denotes the displacement of the main spool, and A_a^m and A_b^m are the effective acting areas of the left and right ends of the main spool, respectively.

Under the action of the pressure difference between the control chambers at both ends, the main spool moves by overcoming the spring force, hydraulic flow force, and viscous damping force, as illustrated in Figure 5. Accordingly, its dynamic equation can be expressed as

$$m^m \frac{\mathrm{d}^2 x^m}{\mathrm{d}t^2} = (p_b^m - p_a^m)A^m - b^m \frac{\mathrm{d}x^m}{\mathrm{d}t} - F_s^m - F_{\mathrm{jet}}^m \tag{7}$$

where m denotes the mass of the main spool, and $A^m \approx A_a^m \approx A_b^m$ denotes the effective acting area of the main spool. b^m is the viscous damping coefficient, and k_s is the spring stiffness. F_{jet} denotes the hydraulic flow force, and F_s^m denotes the spring force acting on the main spool.

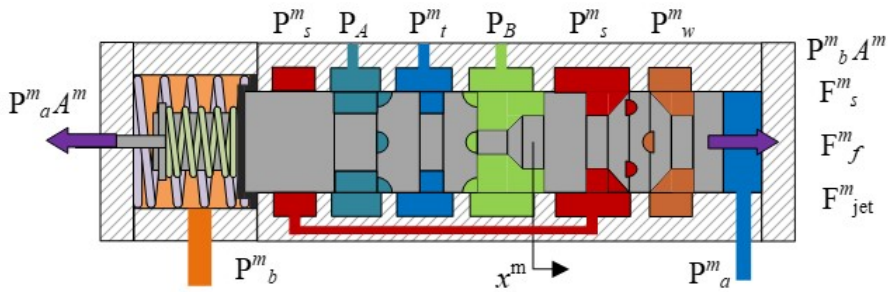


Figure 5. Schematic of the forces acting on the main spool.

The spring force can be expressed as

$$F_s^m = \begin{cases} k_{s,a}^m (l_a + x^m) & , x^m > 0 \\ 0 & , x^m = 0 \\ k_{s,b}^m (x^m - l_b) & , x^m < 0 \end{cases} \tag{8}$$

where $k_{s,a}^m$ and $k_{s,b}^m$ denote the stiffness coefficients of the two return springs acting on the main spool, respectively. l_a and l_b represent the initial compression lengths of the two springs, respectively.

3. Development of the Multiphysics Simulation Model and Nonlinear Characteristic Analysis

3.1. Development of the Multiphysics Co-Simulation Model

Due to the significant magnetic hysteresis, nonlinear electromagnetic force characteristics, and complex hydraulic feedback involved in pilot-stage actuation, conventional analytical modeling methods struggle to achieve both physical fidelity and computational efficiency simultaneously. To more accurately capture the continuous displacement behavior and dynamic response of the main spool under proportional pilot pressure control, the high-fidelity electromagnetic characteristics of the proportional solenoid are extracted using Ansys Electronics. Based on these results, a multiphysics co-simulation model of the two-stage directional valve is developed in the AMESim–Simulink environment, as shown in Figure 6.

In this model, the brown components in the upper part represent the main valve, whereas those in the lower part correspond to the pilot valve. The purple modules denote the proportional solenoids, and the black blocks represent the co-simulation interface between AMESim and Simulink. The blue components indicate the hydraulic source, while the green components represent the spool mass. The key parameters used in the numerical model are listed in Table 1.

A finite-element model of the proportional solenoid is established in Ansys Electronics to investigate the nonlinear characteristics of its complex magnetic circuit [32]. Through numerical simulation, the multidimensional mapping relationships among electromagnetic force, magnetic flux, air gap, and excitation ampere-turns were obtained, as shown in Figure 7.

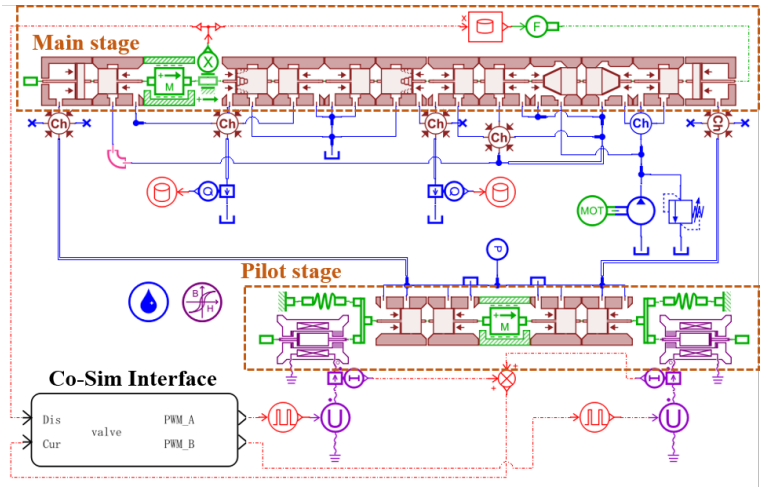


Figure 6. Multi-physics simulation model of pilot-operated directional valve.

Table 1. Key parameters of the simulation model.

Parameters	Value
Oil density (kg/m^3)	850
Kinematic viscosity (m^2/s)	0.000046
Oil temperature (K)	313.15
Pilot supply pressure (bar)	20
Relief pressure (bar)	200
Pilot spool mass (kg)	0.02
Main spool mass (kg)	0.2
Pilot spool diameter (mm)	6
Main spool diameter (mm)	18
Pilot valve orifice diameter (mm)	2

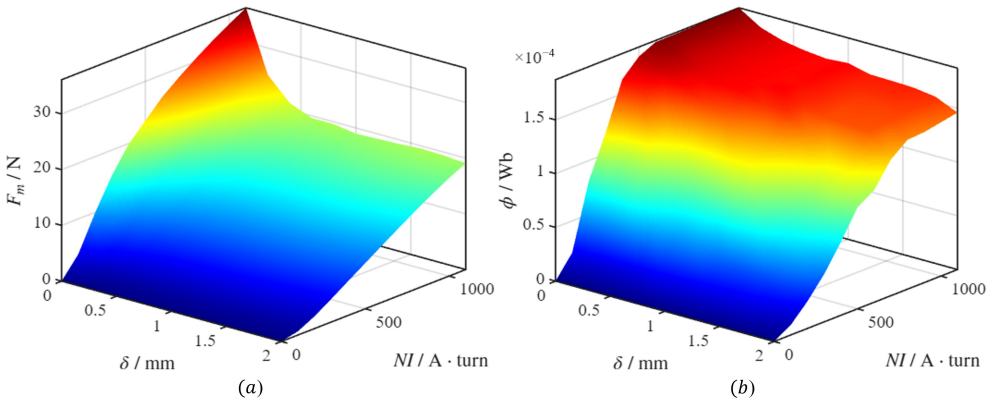


Figure 7. Electromagnetic characteristics of the proportional solenoid. (**a**) Electromagnetic force. (**b**) Magnetic flux. In the figure, the color transition from blue to red indicates increasing values.

The results show that, within the operating air-gap range of 0.5∼2.0 mm, the actuator can generate a maximum electromagnetic force of approximately 20 N, while the peak magnetic flux reaches 1.84×10^{-4} Wb. To enable multiphysics co-simulation, the high-fidelity electromagnetic data were imported into the AMESim electromagnetic actuation module in the form of characteristic files. These data serve as key inputs for analyzing the dynamic characteristics of the pilot stage and the motion behavior of the main spool.

3.2. Nonlinear Characteristic Analysis

3.2.1. Static and Dynamic Characteristics of the Pilot Valve

The pilot valve is the core component of the directional control valve, and its dynamic performance directly determines the overall behavior of the system.

Figure 8a shows the opening and closing responses of the pilot valve under a PWM duty cycle of 50%. The opening time (t_1) is defined as the time required for the spool displacement response to rise from 10% to 90% of its steady-state amplitude, while the closing time (t_2) is defined as the time required for the spool displacement response to fall from 90% to 10% of its steady-state amplitude. As can be observed in the figure, t_1 = 27 ms and t_2 = 56 ms. A noticeable asymmetry between the opening and closing dynamics of the spool can be observed, indicating the presence of inherent nonlinearities and direction-dependent actuation characteristics in the pilot stage. During the movement of the pilot spool, the variation in the magnetic field causes a sudden change in the coil current. This asymmetry is mainly attributed to the coupled electromagnetic and mechanical dynamics of the actuator. During energization, the electromagnetic force increases rapidly as the air gap decreases, thereby accelerating spool motion. In contrast, during de-energization, the coil current decays exponentially because of the inductive effect, and the spool return is mainly driven by the spring force. In addition, hydraulic flow forces and friction further aggravate the dynamic asymmetry.

Figure 8b shows the opening responses of the pilot valve under different duty cycles. It can be seen that the response time does not increase significantly with increasing duty cycle.

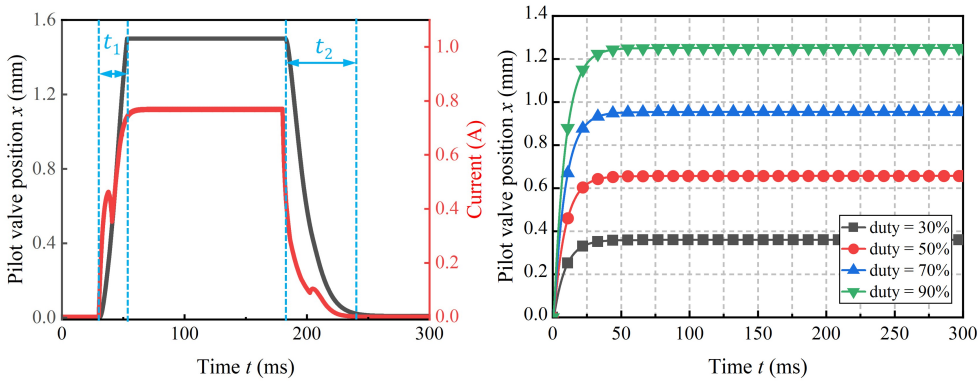


Figure 8. Characteristic curve of the pilot valve. (**a**) Dynamic performance. (**b**) Static performance.

Figure 9 shows the relationship between the PWM duty cycle and the flow rates at working ports *a* and *b*. It can be seen that the pilot valve exhibits pronounced nonlinearity and a significant dead-zone characteristic in its flow response. Owing to the symmetric structure of the valve, the flow trends at ports *a* and *b* are generally consistent. Taking port *b* as a representative example, the duty-cycle range of 45–84% corresponds to a quasi-linear region with stable flow output, whereas the interval of 34–45% represents a nonlinear transition region. When the duty cycle is below 34%, the valve operates in the dead zone, while values above 84% indicate the onset of saturation. It should be noted that the identified dead zone arises not only from the inherent structural characteristics of the valve, such as overlap and manufacturing tolerances, but also from additional nonlinear effects introduced by current input dynamics, friction, and other coupled factors. The nonlinear transition region occurs because the input signal is insufficient to fully open or fully close the valve, resulting in a partially open or partially closed state. In addition, the dead zone and saturation region correspond to the conditions in which the valve cannot open and cannot further increase its opening, respectively.

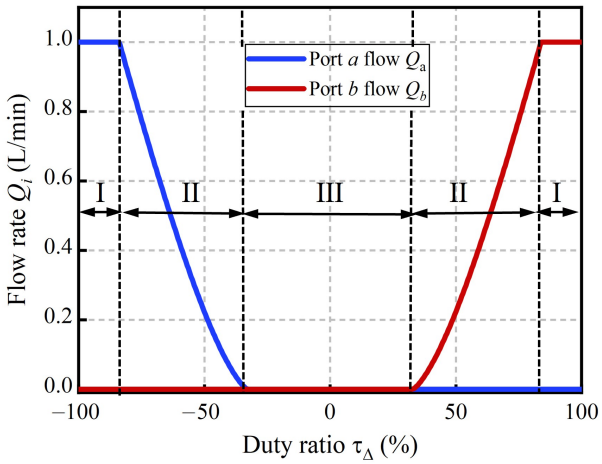


Figure 9. Flow characteristic curve.

3.2.2. Static and Dynamic Characteristics of the Main Valve

Figure 10a shows the motion characteristics of the main spool under different PWM duty cycles. It can be seen that when the duty cycle exceeds a certain threshold, the main spool exhibits a consistent dynamic response trend; otherwise, no noticeable motion occurs. This phenomenon is mainly attributed to the dead zone of the pilot stage, within which no effective pressure differential can be established in the control chambers of the main valve. Once the dead zone is overcome, the relationship between duty cycle and spool displacement follows a similar trend under different inputs, although quantitative differences still exist. Taking the 50% and 70% duty cycles as representative cases, the rise times are approximately 92 ms and 42 ms, respectively. A higher duty cycle leads to a faster displacement response, mainly because a larger flow rate is delivered per unit time.

When the main spool reaches its mechanical end position, its motion is constrained by the physical stop and therefore comes to a halt. At this point, the pressure in the control chamber of the main spool rapidly rises to the pilot supply pressure, as shown in Figure 10b. In addition, the pressure exhibits a two-stage increase, which is attributed to the sudden engagement of the return spring. In the first stage, the spring force is relatively small when it initially takes effect, resulting in a rapid pressure rise. In the second stage, as the spring resistance increases, the pressure rise becomes more gradual. A higher duty cycle results in a larger abruptly applied electromagnetic force, which accelerates spool motion and causes the second pressure-rise stage to begin earlier.

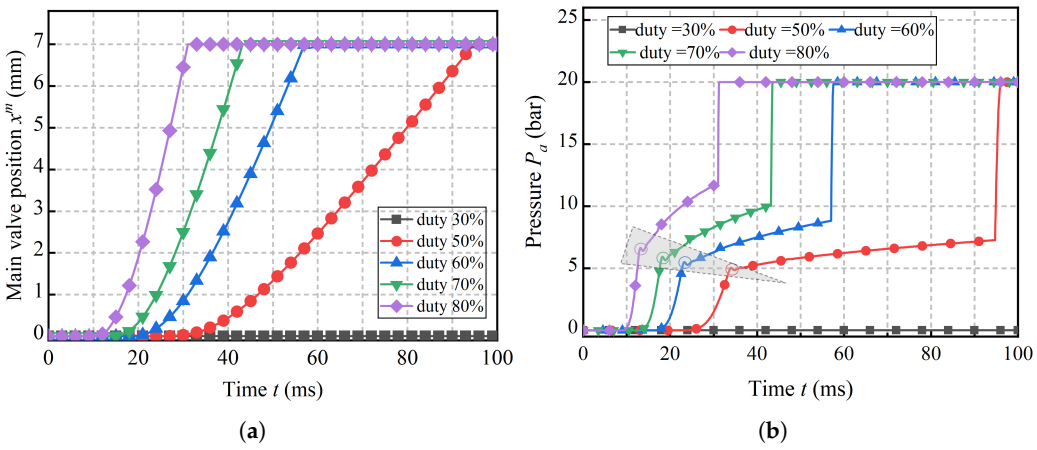


Figure 10. Characteristic curves of the main valve. (**a**) Displacement characteristic. (**b**) Pressure characteristic.

3.2.3. Dead-Zone and Hysteresis Characteristics

To further identify the dead-zone range, the duty cycle at which the main spool displacement exceeds a prescribed threshold is first adopted as an indicator of the dead zone. The duty cycle applied to the pilot valve is increased incrementally while the state of the main spool is monitored. After the main spool remains stable at its limit position for a certain period, the duty cycle is gradually reduced. The corresponding results are shown in Figure 11. As can be seen, the dead-zone range is located between $t_1' = -34.5\%$ and $t_1 = 34.5\%$. From a numerical point of view, the dead zone of the directional valve is nearly symmetric.

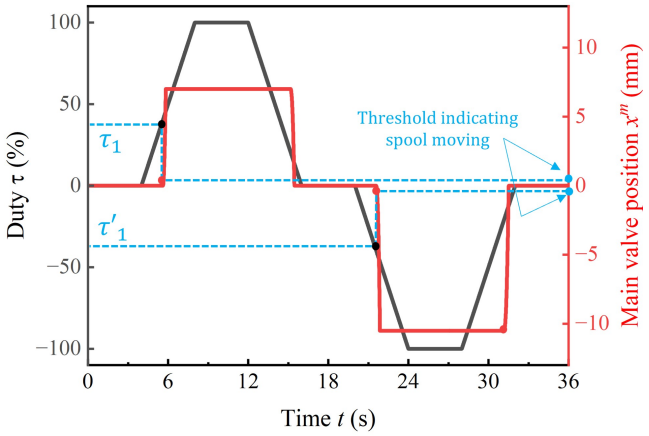


Figure 11. Duty-cycle curves during the opening and closing processes of the main valve.

4. Design of the DBO-Optimized Fuzzy PID Controller

4.1. Closed-Loop Position Control Architecture

Based on the dynamic characteristics of both the pilot valve and the main spool, this study proposes a dung-beetle-optimizer-based fuzzy PID control strategy (DBO-FPID) to determine the required duty-cycle increment, τ_Δ, for the pilot valve. The fuzzy PID (FPID) controller adjusts its parameters according to the position error and its rate of change, thereby alleviating the limitations of fixed-parameter PID control. However, the performance of the FPID controller strongly depends on the proper selection of scaling factors and quantization factors, which are usually tuned manually in a process that is time-consuming and highly dependent on expert experience. To overcome this limitation, the dung beetle optimizer is introduced to optimize these parameters and improve the tuning efficiency. DBO provides a good balance between global exploration and local exploitation, and has shown favorable convergence speed and search capability in solving nonlinear optimization problems, while also exhibiting good potential for avoiding local optima.

Figure 12 shows the schematic of the proposed control strategy. The control scheme generates the control output, τ_Δ, in real time according to the position error e and its derivative $\dot{e}$. The control architecture consists of three layers. The inner layer is a PID controller, the middle layer is the FPID controller, and the outer layer is the DBO-based optimization module. The DBO algorithm uses the position error e and its derivative $\dot{e}$ to optimize both the initial PID parameters and the scaling and quantization factors of the FPID controller. Meanwhile, the FPID controller adaptively generates correction terms based on e and $\dot{e}$. Through the integration of these layers, the proposed control strategy can effectively cope with system nonlinearities, such as dead-zone effects, and improve the overall control performance.

It should be noted that the DBO algorithm is used only for offline parameter tuning and does not participate in the closed-loop control process. Therefore, the system stability

is mainly determined by the fuzzy PID controller. The controller designed in this study can be regarded as a bounded variable-gain PID controller. Under bounded control gains and within the specified operating range, the system response remains bounded. In addition, both simulation and experimental results show that no sustained oscillation or divergence occurs, further verifying the stability of the proposed control strategy.

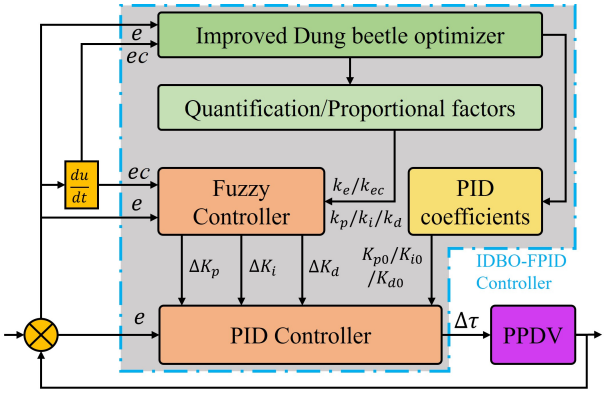


Figure 12. Block diagram of the spool position control strategy.

4.2. Design of the Fuzzy PID Controller

4.2.1. Fuzzy Inference Mechanism and Rule Design

In the FPID controller, the control output τ_Δ is expressed as a linear combination of the proportional, integral, and derivative terms of the position error e. However, unlike the conventional PID controller, the fuzzy inference mechanism adaptively adjusts the PID parameters according to the error e and its rate of change ec through fuzzification and rule-based reasoning. The corresponding control law can be written as follows:

$$\tau_\Delta = (K_{p0} + \Delta K_p)e(t) + (K_{i0} + \Delta K_i)\int_0^t e(t)dt + (K_{d0} + \Delta K_d)\frac{de(t)}{dt} \tag{9}$$

where K_{p0}, K_{i0}, and K_{d0} denote the initial PID parameters, and ΔK_p, ΔK_i, and ΔK_d denote the corresponding adjustment terms. The input variables e and $\dot{e}$ of the fuzzy controller are normalized to the range $[-1, 1]$, and the output variables are also normalized to $[-1, 1]$. Both the input and output variables are divided into seven fuzzy subsets, namely NB, NM, NS, ZE, PS, PM, and PB. The membership functions of the input and output variables are shown in Figure 13. The scaling factors for the input variables e and $\dot{e}$ are defined as k_e and k_{ec}, respectively, whereas the output scaling factors for ΔK_p, ΔK_i, and ΔK_d are defined as k_p, k_i, and k_d, respectively. The fuzzy inference process is implemented using the Mamdani method, and defuzzification is performed using the centroid method. The fuzzy rule base is given in Table 2.

Table 2. Fuzzy rule table for ΔK_p, ΔK_i, and ΔK_d.

$e\backslash\dot{e}$	NB	NM	NS	ZE	PS	PM	PB
NB	[PB, NB, PS]	[PB, NM, PS]	[PM, NM, ZE]	[PM, NS, ZE]	[PS, ZE, NS]	[ZE, ZE, NS]	[ZE, PS, NB]
NM	[PB, NB, PS]	[PM, NM, PS]	[PM, NS, ZE]	[PS, NS, ZE]	[ZE, ZE, NS]	[ZE, PS, NM]	[NS, PS, NB]
NS	[PM, NM, ZE]	[PM, NS, ZE]	[PS, NS, NS]	[ZE, ZE, NS]	[NS, ZE, NM]	[NM, PS, NB]	[NM, PM, NB]
ZE	[PM, NS, ZE]	[PS, NS, ZE]	[ZE, ZE, NS]	[ZE, ZE, ZE]	[ZE, ZE, NS]	[NS, PS, NM]	[NM, PM, NB]
PS	[PS, ZE, NS]	[ZE, ZE, NS]	[NS, ZE, NM]	[NM, ZE, NS]	[NM, NS, NM]	[NM, PM, NB]	[NB, PB, NB]
PM	[ZE, PS, NS]	[NS, PS, NM]	[NM, PS, NB]	[NM, NS, NB]	[NB, NS, NB]	[NB, PM, NB]	[NB, PB, NB]
PB	[ZE, PS, NB]	[ZE, PM, NB]	[NM, PM, NB]	[NB, PM, NB]	[NB, NS, NB]	[NB, PB, NB]	[NB, PB, NB]

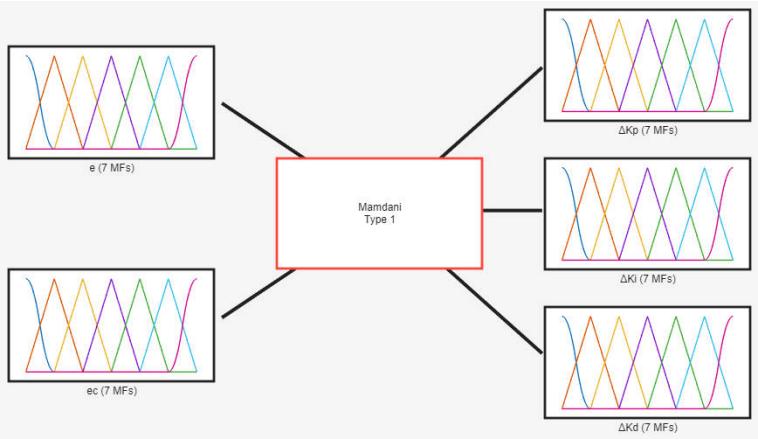


Figure 13. Membership functions of the input and output variables.

The integral of time-weighted absolute error (ITAE) is selected as the objective function because it assigns a greater penalty to errors occurring at later stages of the response, thereby promoting faster error attenuation while maintaining steady-state accuracy. This makes it particularly suitable for characterizing and optimizing dynamic performance indices such as switching lag and dead-zone residence time under dead-zone nonlinearity. The objective function is defined as

$$ITAE = \int_0^{t_f} t|e(t)|\,dt \tag{10}$$

where t denotes the system operating time, and t_f denotes the evaluation time horizon, which is set to 1 s in this study. And $|e(t)|$ denotes the absolute error between the reference value and the actual displacement of the main spool. Equation (10) is used as the fitness function to evaluate each individual. A smaller ITAE value indicates better control performance and a response closer to the desired one.

4.2.2. Controller Parameter Optimization Using DBO

The dung beetle optimizer (DBO) is a swarm intelligence algorithm introduced in 2022 [33], inspired by the behaviors of dung beetles. Specifically, the algorithm is designed based on four key activities of dung beetles: ball rolling, reproduction, foraging, and stealing. Figure 14 shows the flowchart of the DBO algorithm. The procedure begins with the random initialization of the dung beetle population within the search space, together with the specification of the relevant parameters. The fitness value of each individual is then evaluated, and the optimization process is iteratively carried out until the stopping criterion is satisfied. The detailed mathematical formulation is given as follows:

(1) Ball-rolling dung beetle

In the absence of obstacles, ball-rolling dung beetles maintain approximately straight-line motion by relying on celestial cues. The position update process can be described as follows:

$$x_i(t+1) = x_i(t) + akx_i(t-1) + b|x_i(t) - x_w(t)| \tag{11}$$

where $x_i(t)$ denotes the position of the i-th individual at iteration i; a denotes the influence of environmental disturbances that cause deviations from the original moving direction; k denotes a directional adjustment factor; $b \in (0,1]$ denotes a random variable; and $x_w(t)$ denotes the worst position in the current population. The term $|x_i(t) - x_w(t)|$ denotes introduced to model variations in light intensity, where larger values correspond to weaker illumination.

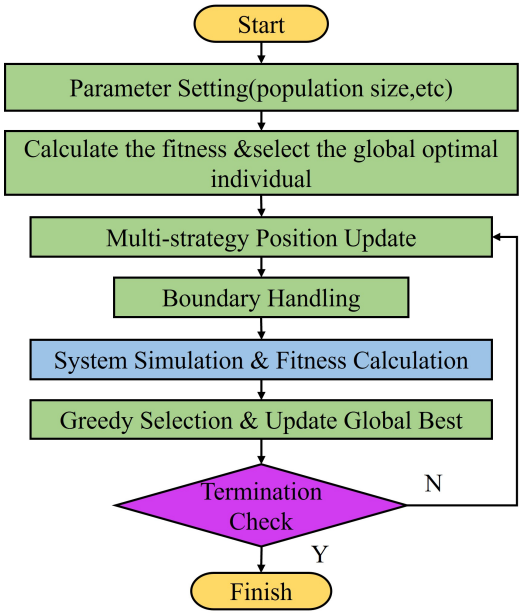


Figure 14. The DBO optimisation process.

When obstacles are encountered, dung beetles adjust their moving direction through a characteristic dancing behavior, which is modeled by a tangent function. The corresponding position update rule can be expressed as follows:

$$x_i(t+1) = x_i(t) + \tan(\theta)\,|x_i(t) - x_i(t-1)| \tag{12}$$

where $\theta \in [0, \pi]$ denotes the deviation angle. When $\theta = 0$ or $\theta = \frac{\pi}{2}$, the individual remains stationary. The term $|x_i(t) - x_i(t-1)|$ denotes the positional displacement of the i-th individual between two consecutive iterations.

(2) Reproductive dung beetles

A boundary selection strategy is employed to model the spawning region of female dung beetles, and the corresponding position update is formulated as follows:

$$x_i(t+1) = X^*(t) + b_1\left(x_i(t) - L_b^*\right) + b_2\left(x_i(t) - U_b^*\right) \tag{13}$$

where $X^*(t)$ denotes the global best position at iteration t; b_1 and b_2 denote two independent random vectors of dimension $1 \times d$, where d denotes the dimension of the optimization problem; L_b^* and U_b^* denote the lower and upper bounds of the spawning region, respectively.

$$\begin{aligned} Lb^* &= \max\left(X^* \times (1-R),\, Lb\right) \\ Ub^* &= \max\left(X^* \times (1+R),\, Ub\right) \end{aligned} \tag{14}$$

where X^* denotes the current local best position at the current iteration. $R = 1 - t/T_{\max}$, with $T_{\max}$ denotes the predefined maximum number of iterations. Lb and Ub denote the lower and upper bounds of the optimization problem, respectively.

During the iterative process, the boundaries of the spawning region and the positions of the egg balls change dynamically. The corresponding update rule is given as follows:

$$B_i(t+1) = X^* + b_1 \times \left(B_i(t) - Lb^*\right) + b_2 \times \left(B_i(t) - Ub^*\right) \tag{15}$$

where $B_i(t)$ denotes the position of the i-th egg ball at the t-th iteration. b_1 and b_2 denote two independent random vectors of size $1 \times d$, where d denotes the dimensionality of the optimization problem.

(3) Foraging dung beetles

The offspring hatch and transform into foraging individuals, which move toward promising feeding areas. Their position update during the foraging process can be expressed as follows:

$$x_i(t+1) = x_i(t) + C_1\left(x_i(t) - L_b^b\right) + C_2\left(x_i(t) - U_b^b\right) \tag{16}$$

where C_1 denotes a random number that follows a normally distributed, and C_2 denotes a random vector belonging to $(0, 1)$. L_b^b and U_b^b denote the lower and upper bounds of the foraging region, respectively. The boundary of the optimal foraging area is defined as follows:

$$\begin{aligned} Lb^b &= \max\left(X^* \times (1 - R),\, Lb\right) \\ Ub^b &= \max\left(X^* \times (1 + R),\, Ub\right) \end{aligned} \tag{17}$$

where X_b denotes the global best position.

(4) Stealing dung beetles

During the foraging process, some individuals exhibit stealing behavior by competing for resources with others. The corresponding position update rule is given as follows:

$$x_i(t+1) = X^b(t) + S \times g \times \left(\left|x_i(t) - X^*(t)\right| + \left|x_i(t) - X^b(t)\right|\right) \tag{18}$$

where $X^b(t)$ denotes the best food source at iteration t; S denotes a constant coefficient; and g denotes a $1 \times d$ random vector obeying a normal distribution.

The total number of dung beetles in both stages is set to 40, among which the numbers of the four categories of individuals are 8, 8, 11, and 13, respectively. The maximum number of iterations is set to 40. The termination criterion was defined as reaching the maximum iteration number. When optimizing the PID controller, the position vector of each dung beetle is set to dimension 3, and the search ranges of the optimization parameters K_p, K_i, and K_d are defined as [1, 300], [1, 600] and [0.01, 5], respectively. When optimizing the FPID controller, the position vector of each dung beetle is set to dimension 5, and the search ranges of the optimization parameters k_p, k_i, k_d, k_e, and k_{ec} are defined as [0, 20], [0, 40], [0, 5], [0, 5], and [0, 1], respectively.

4.2.3. Comparison of Optimization Algorithms

To further demonstrate the performance of the DBO employed in this study for parameter optimization, a comparative investigation was conducted among several representative metaheuristic optimization algorithms. PSO, GWO, and SSA were selected as benchmark methods. Under identical optimization conditions, including the same population size, maximum number of iterations, and search boundaries, experimental tests were carried out using the F6 test function from the CEC 2022 single-objective bound-constrained numerical optimization benchmark suite [34]. This test function belongs to the category of hybrid functions (Hybrid Function 1) and is capable of effectively reflecting the global search capability, convergence speed, and ability of an optimization algorithm to avoid being trapped in local optima in a complex nonlinear search space.

For clarity, the principal parameter settings of the four optimization algorithms are briefly summarized as follows. For PSO, the acceleration coefficients are set to $c_1 = c_2 = 2$, the inertia weight is set to $\omega = 0.8$, and the maximum velocity is defined as $v_{max} = 6$. For GWO, the lower and upper bounds of the control parameter are set to $a_{min} = 0$ and $a_{max} = 2$, respectively. For SSA, the producer update probability is set to 0.5, and the initial velocity is set to $v_0 = 0$. For DBO, the parameters are chosen as k = 0.1, b = 0.3, and S = 0.5.

Figure 15 presents the fitness convergence curves of the different optimization algorithms under the same experimental conditions. It can be observed that DBO exhibits a faster rate of fitness reduction during the early stage of iteration and converges to a better solution within fewer iterations. By contrast, although PSO demonstrates a certain degree of search capability in the initial stage, its convergence trend gradually becomes flatter in the later stage, indicating a degree of stagnation. The fitness reduction process of GWO is relatively slow throughout the optimization process, and its final convergence result is inferior to that of DBO. SSA shows relatively rapid convergence in the initial stage; however, its search efficiency decreases during the middle and later stages of the optimization process. Overall, DBO outperforms the other comparative algorithms in terms of both convergence efficiency and final optimization performance.

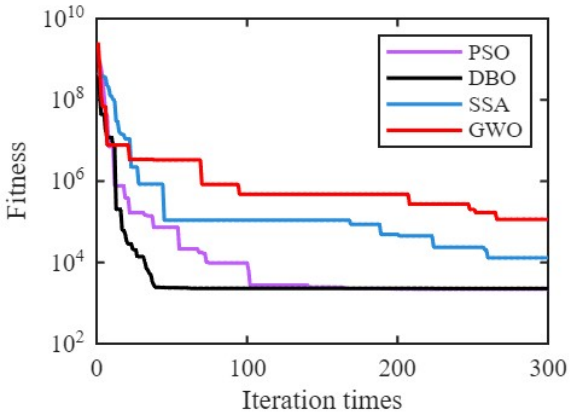


Figure 15. The convergence curves by the DBO algorithm and other optimizers on benchmark test functions.

4.3. Simulation-Based Comparative Analysis

To verify the effectiveness of the proposed control strategy for spool position control of the two-stage hydraulic directional valve, a co-simulation model was established in the Simulink–AMESim environment, as shown in Figure 16.

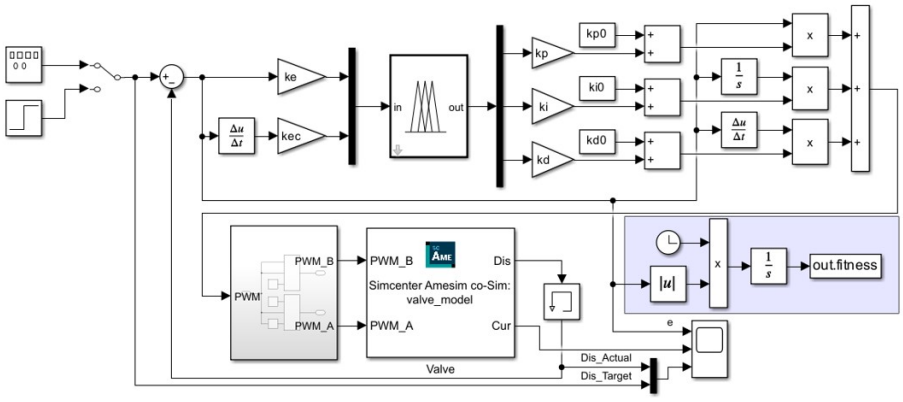


Figure 16. Co-simulation model of the pilot-operated proportional directional valve.

Figure 17 presents the iterative optimization curves. The selected algorithm can rapidly optimize the three PID parameters as well as the correction coefficients of the fuzzy PID controller. Both fitness functions exhibit a clear decreasing trend and converge rapidly, reaching stable minimum values within fewer than 10 iterations. Among them, the converged values of K_p, K_i and K_d are 194.53, 324.62 and 0.62, respectively. The converged values of the fuzzy PID output scaling factors k_p, k_i and k_d are 11.51, 24.64 and 2.46, respectively. The converged values of the quantization factors k_e and k_{ec} are 0.58 and 0.44,

respectively. These results demonstrate that the DBO algorithm has strong optimization capability and fast convergence performance.

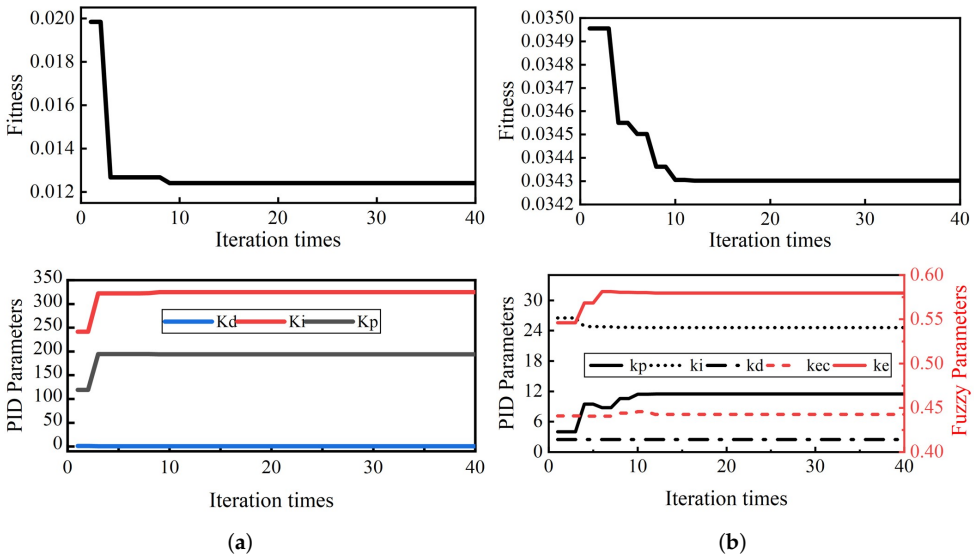


Figure 17. Parameter optimisation results. (**a**) DBO-PID. (**b**) DBO-FPID.

Figure 18 shows the step response tracking curves. At $t = 0.5$ s, a step control signal of 6 mm is applied. The result shows that neither method exhibits significant overshoot, and both achieve a similar steady-state error of approximately 0.06 mm. However, compared with the DBO-PID control strategy, the DBO-FPID control strategy reduces the rise time from 68 ms to 31 ms, corresponding to an improvement of approximately 54.4%. The shorter response time helps mitigate the switching delay during the directional control process, while the steady-state error remains at 0.08 mm.

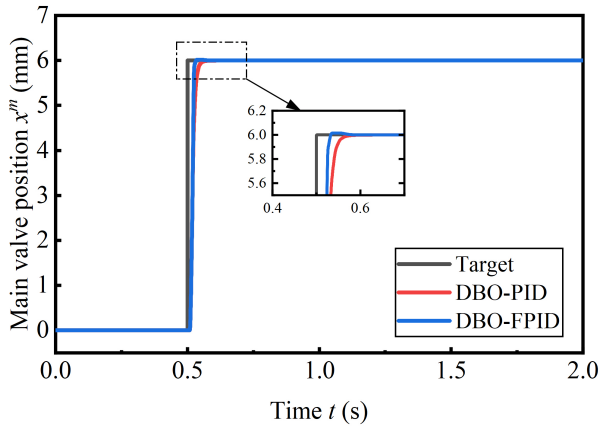


Figure 18. Main spool displacement tracking response under step input.

To further evaluate the switching performance of the directional valve under the proposed control strategy, triangular and sinusoidal reference signals are applied. Figure 19a shows the tracking response and tracking error under the triangular input. As discussed previously, the dead-zone effect causes a noticeable lag during the switching process. When crossing the zero position, the DBO-FPID control strategy significantly alleviates the switching delay. The time interval during which the displacement remains at zero is defined as the dead-zone residence time and used as a performance index. Compared with the DBO-PID control strategy, the DBO-FPID approach reduces the dead-zone residence time from 40 ms to 21 ms, corresponding to an improvement of approximately 47.5%. In

addition, the tracking error of the DBO-FPID control strategy is consistently smaller than that of the DBO-PID control strategy.

Figure 19b shows the tracking response and tracking error under the sinusoidal input. Similar to the triangular-input case, the dead-zone effect also causes an evident lag during switching. Compared with the DBO-PID control strategy, the DBO-FPID approach reduces the dead-zone residence time from 29 ms to 16 ms, corresponding to an improvement of approximately 44.8%. The tracking error of the DBO-FPID control strategy also remains consistently smaller than that of the DBO-PID strategy.

Further analysis of the simulation results is carried out using the root mean square error (RMSE), maximum error, and mean absolute error (MAE). The detailed performance metrics are summarized in Table 3. The results indicate that the DBO-FPID control strategy effectively mitigates the switching lag of the directional valve while maintaining high control accuracy.

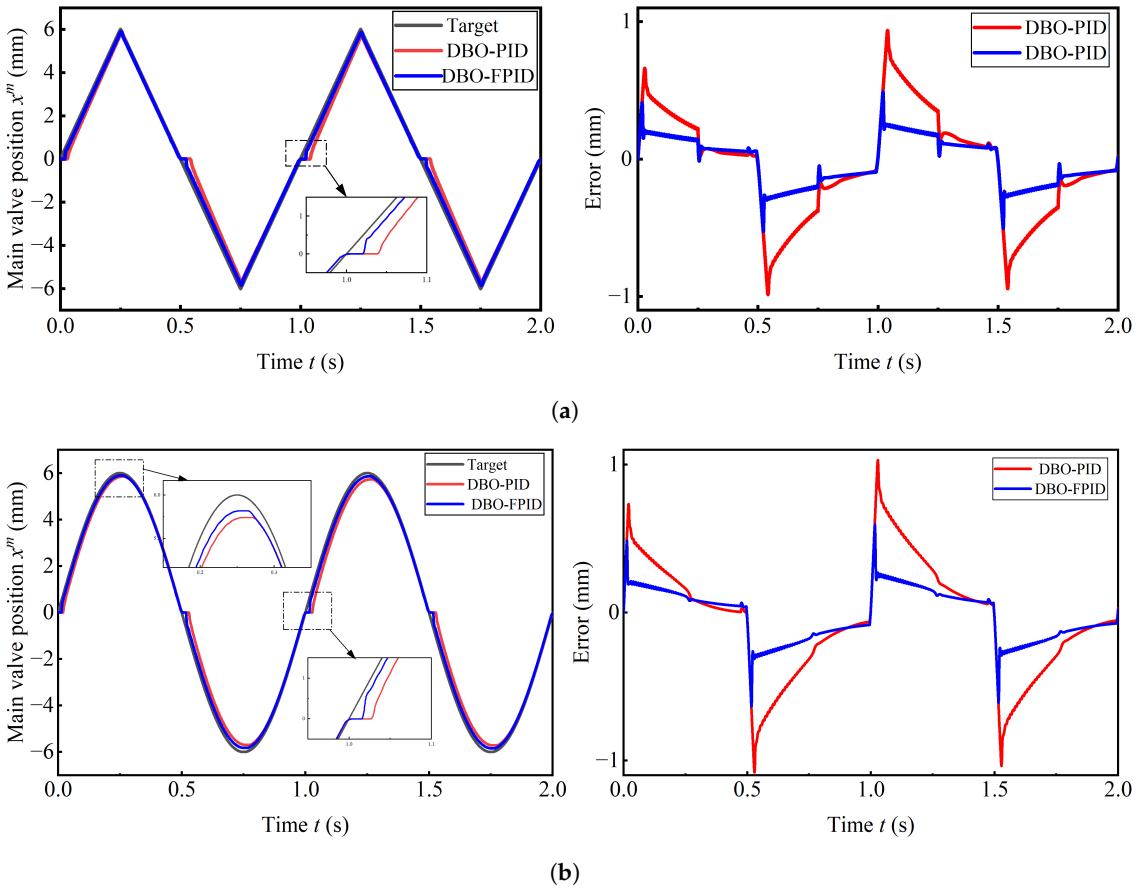


Figure 19. Main spool position tracking curve under typical excitations. (**a**) Triangular wave. (**b**) Sinusoidal wave.

Table 3. Position tracking performance of the main spool under typical excitations.

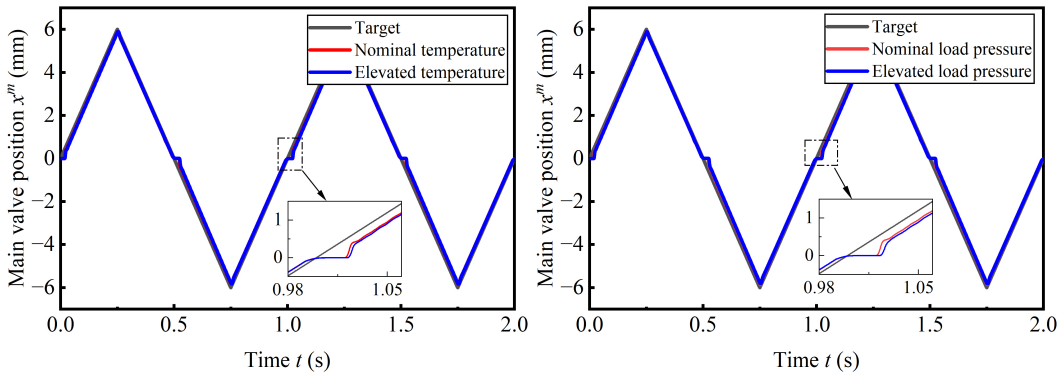
Control Strategies	Excitation Signal	Maximum Error	Residence Time	Mean Absolute Error	RMSE
DBO-PID	Sinusoidal wave	1.032 mm	29 ms	0.031 mm	0.037 mm
	Triangular wave	0.921 mm	40 ms	0.030 mm	0.038 mm
DBO-FPID	Sinusoidal wave	0.598 mm	16 ms	0.015 mm	0.017 mm
	Triangular wave	0.527 mm	21 ms	0.014 mm	0.018 mm

The dynamic characteristics of hydraulic systems are highly sensitive to variations in oil temperature and load pressure. To further evaluate the robustness of the proposed

DBO-FPID controller under parameter perturbations, simulation analyses were performed under oil-viscosity variation and load-pressure variation conditions. In this study, the influence of increased oil temperature on the system dynamics was equivalently represented by reducing the oil viscosity, whereas the controller's adaptability to external pressure disturbances was examined by varying the load pressure at the valve port. A triangular reference displacement signal with a frequency of 1 Hz and an amplitude of 6 mm was used as the target trajectory in the simulations.

Figure 20a,b show the displacement tracking curves when the oil viscosity is reduced by 10%, and the valve-port pressure is increased by 10%, respectively. The results indicate that when the system parameters deviate from the nominal operating condition, the dynamic performance of the proposed DBO-FPID controller exhibits slight degradation, mainly manifested as a slightly slower response and a small increase in tracking error. Nevertheless, the closed-loop system response remains bounded, and no sustained oscillation or divergence is observed, indicating that the control parameters optimized by DBO remain effective within a certain range of oil-viscosity variation and load-pressure disturbance. Under the oil-temperature variation and load-pressure variation conditions, the dead-zone residence time increased by only 2 ms and 3 ms, respectively. In addition, the increases in the maximum tracking error, root mean square error, and mean absolute error were limited to 0.134 mm and 0.152 mm, 0.028 mm and 0.034 mm, and 0.009 mm and 0.012 mm, respectively. These results indicate that the performance degradation caused by parameter perturbations is relatively small.

These results demonstrate that the proposed DBO-FPID controller exhibits a certain degree of robustness against parameter variations in the hydraulic system.



(**a**) (**b**)

Figure 20. Main spool position tracking curves under parameter perturbation conditions. (**a**) Elevated temperature. (**b**) Elevated load pressure disturbance.

5. Experimental Validation

5.1. Experimental Setup and Test Procedure

To validate the position control performance of the DBO-FPID control strategy for the two-stage directional valve, an experimental platform was established, as shown in Figure 21. The hydraulic test bench is a dedicated platform for directional valve testing, integrating a hydraulic power supply and multiple pipeline interfaces with flexible and adjustable operating parameters. According to the working principle of the directional valve, the hydraulic circuit was connected as illustrated in Figure 21. The displacement sensor and its demodulation circuit are integrated into the controller. During the experiments, the main spool displacement was sampled by the internal ADC of the microcontroller in the controller, and then transmitted to the host computer via CAN communication at a frequency of 1 kHz. Since this study mainly focuses on the relative performance differences among

different control strategies under the same hardware platform and consistent operating conditions, all comparative experiments were conducted with the same sampling period, communication link, and testing procedure, so as to minimize the influence of measurement and transmission errors on the comparative conclusions. In the dedicated hydraulic valve test bench, No. 46 anti-wear hydraulic oil was used. During system operation, the oil temperature was maintained at 50 ± 5 °C, the supply pressure of the two-stage directional valve was kept at 20 MPa, and the load pressure was kept at 10 MPa.

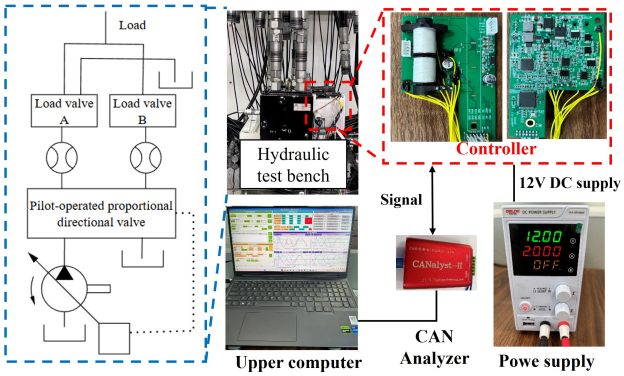


Figure 21. Experimental test bench and testing principle.

5.2. Experimental Results and Discussion

Figure 22 presents the experimental tracking results. The results show that the spool of the directional valve can effectively track the reference displacement signal under the DBO-FPID control strategy. Figure 22a shows the response to a triangular reference signal with a frequency of 1 Hz and an amplitude of 6 mm. The dead-zone residence time is approximately 30 ms, the root mean square error (RMSE) is 0.262 mm, the maximum error is 1.053 mm, and the mean absolute error (MAE) is 0.197 mm. The RMSE in the experiment is larger than that in the simulation because friction and hydraulic disturbances are present in the physical system. Figure 22b shows the response to a triangular reference signal with a frequency of 0.5 Hz and an amplitude of 6 mm. The dead-zone residence time is approximately 26 ms, the RMSE is 0.121 mm, the maximum error is 0.497 mm, and the MAE is 0.091 mm. Overall, the experimental results are in good agreement with the simulation results, validating the effectiveness of the proposed control strategy.

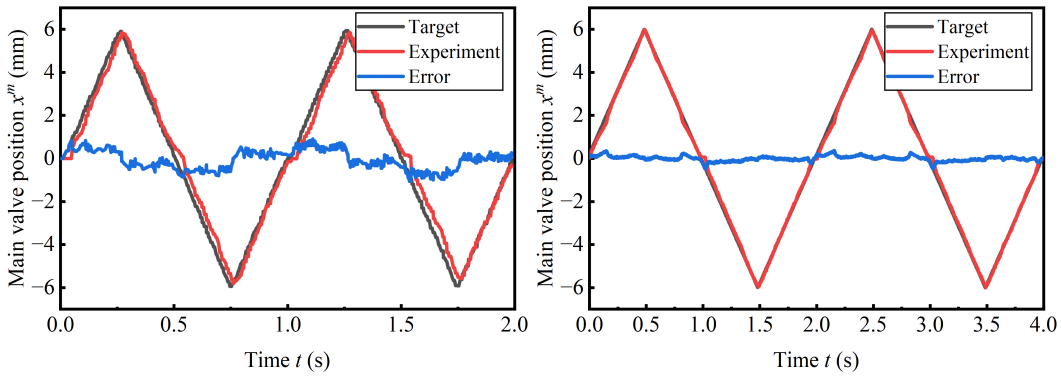


Figure 22. Main spool position tracking curve under different frequency sinusoidal excitation signals: (**a**) 1 Hz and (**b**) 0.5 Hz.

6. Conclusions

This study investigated the high-precision position control problem of pilot-operated proportional directional valves under dead-zone nonlinearity. A fuzzy PID control strategy

optimized by the dung beetle optimizer (DBO-FPID) was proposed. The results show that the proposed method can improve control accuracy, reduce dead-zone residence time, mitigate switching lag, and enhance system robustness. The main conclusions are summarized as follows:

(1) By considering the structural characteristics of the valve and its dynamic response mechanism, the dead-zone range and its influence on system hysteresis and tracking performance were analyzed. A refined nonlinear model combining AMESim simulation and theoretical analysis was established, enabling a quantitative characterization of the dead-zone evolution mechanism. The dead-zone range of the directional valve was identified as $\pm 34.5\%$ duty cycle, which provides a theoretical basis for the design of fuzzy control rules.

(2) A DBO-FPID control strategy was proposed to improve the dynamic response during the dead-zone crossing process, thereby reducing the response lag and residence time near the dead zone while enhancing position tracking accuracy. The comparative simulation results demonstrate the advantages of the proposed DBO-FPID controller over DBO-PID in terms of transient response and dead-zone crossing performance. The rise time under step input is reduced by 54.4%, while the dead-zone residence times under triangular and sinusoidal inputs are reduced by 47.5% and 44.8%, respectively. Meanwhile, the mean absolute error remains below 0.2 mm, indicating satisfactory tracking accuracy. Experimental results further verify the feasibility and effectiveness of the proposed controller on the physical valve platform.

(3) To evaluate the robustness of the proposed algorithm, simulation experiments were carried out under oil-temperature and pressure variations. The results demonstrate that the proposed DBO-FPID controller can maintain a certain degree of robustness against hydraulic system parameter variations.

Although the proposed DBO-FPID control strategy achieves satisfactory control performance under dead-zone nonlinearity, several issues still deserve further investigation. First, the DBO adopted in this study is mainly used for offline tuning. In future work, it may be combined with online parameter identification, adaptive adjustment, or gain-scheduling methods to further improve the controller's adaptability to complex operating conditions. Second, the real-time implementation of the proposed method on embedded platforms, the optimization of computational complexity, and the evaluation of long-term operational stability also remain important challenges for future engineering applications.

Author Contributions: Conceptualization, H.G.; methodology, H.G.; software, H.G.; validation, H.G. and H.Z.; formal analysis, H.G.; investigation, H.G., H.C. and B.L.; data curation, H.G.; writing—original draft preparation, H.G.; writing—review and editing, B.S.; visualization, H.G.; supervision, B.S.; project administration, B.S. All authors have read and agreed to the published version of the manuscript.

Funding: This research was funded by the National Natural Science Foundation of China, grant number 51875035.

Institutional Review Board Statement: Not applicable.

Informed Consent Statement: Not applicable.

Data Availability Statement: The original contributions presented in the study are included in the article; further inquiries can be directed to the corresponding author.

Acknowledgments: The authors would like to thank Boqiang Shi for valuable guidance and constructive suggestions throughout this study. The authors also thank the laboratory members for their assistance with the experimental setup and data collection.

Conflicts of Interest: The authors declare no conflicts of interest.

References

1. Li, S.; Du, J.; Shi, Z.; Xu, K.; Shi, W. Characteristics analysis of the pilot-operated proportional directional valve by experimental and numerical investigation. *Energies* **2022**, *15*, 9418. [CrossRef]
2. Xu, B.; Shen, J.; Liu, S.; Su, Q.; Zhang, J. Research and development of electro-hydraulic control valves oriented to industry 4.0: A review. *Chin. J. Mech. Eng.* **2020**, *33*, 29. [CrossRef]
3. Zhong, Q.; Xu, E.G.; Jia, T.W.; Yang, H.Y.; Zhang, B.; Li, Y.B. Dynamic performance and control accuracy of a novel proportional valve with a switching technology-controlled pilot stage. *J. Zhejiang Univ.-Sci. A* **2022**, *23*, 272–285. [CrossRef]
4. Gao, B.; Zhang, W.; Zheng, L.; Zhao, H. Research on high-precision position control of valve-controlled cylinders based on variable structure control. *Machines* **2023**, *11*, 623. [CrossRef]
5. Li, Y.; Li, R.; Yang, J.; Xu, J.; Yu, X. Recent advances in control strategies and algorithms for pilot-operated electro-hydraulic proportional directional valves. *Proc. Inst. Mech. Eng. Part E J. Process Mech. Eng.* **2025**, *239*, 3881–3902. [CrossRef]
6. Su, Q. Switching Delay Analysis and Compensation Methods for the Pilot Operated Proportional Directional Valves. Ph.D. Thesis, Zhejiang University, Hangzhou, China, 2016.
7. Zhang, J.; Lu, Z.; Xu, B.; Su, Q. Investigation on the dynamic characteristics and control accuracy of a novel proportional directional valve with independently controlled pilot stage. *ISA Trans.* **2019**, *93*, 218–230. [CrossRef]
8. Xu, B.; Su, Q.; Zhang, J.; Lu, Z. Analysis and compensation for the cascade dead-zones in the proportional control valve. *ISA Trans.* **2017**, *66*, 393–403. [CrossRef]
9. Lu, Z.; Zhang, J.; Xu, B.; Wang, D.; Su, Q.; Qian, J.; Yang, G.; Pan, M. Deadzone compensation control based on detection of micro flow rate in pilot stage of proportional directional valve. *ISA Trans.* **2019**, *94*, 234–245. [CrossRef]
10. Stosiak, M.; Karpenko, M.; Ivannikova, V.; Maskeliūnaitė, L. The impact of mechanical vibrations on pressure pulsation, considering the nonlinearity of the hydraulic valve. *J. Low Freq. Noise, Vib. Act. Control* **2025**, *44*, 706–719. [CrossRef]
11. Stosiak, M.; Karpenko, M.; Deptuła, A.; Urbanowicz, K.; Skačkauskas, P.; Cieślicki, R.; Deptuła, A.M. Modelling and Experimental verification of the interaction in a hydraulic directional control valve spool pair. *Appl. Sci.* **2022**, *13*, 458. [CrossRef]
12. Ma, W.; Ma, S.; Qiao, W.; Cao, D.; Yin, C. Research on PID controller of excavator electro-hydraulic system based on improved differential evolution. *Machines* **2023**, *11*, 143. [CrossRef]
13. Venkaiah, P.; Sarkar, B.K. Electrohydraulic proportional valve-controlled vane type semi-rotary actuated wind turbine control by feedforward fractional-order feedback controller. *Proc. Inst. Mech. Eng. Part I J. Syst. Control Eng.* **2022**, *236*, 318–337. [CrossRef]
14. Tao, H.; Niu, H.X.; Duo-wang, F. Simulation and experiment study of optimizational PID control with changing integration rate. *TELKOMNIKA Indones. J. Electr. Eng.* **2013**, *11*, 550–558. [CrossRef]
15. Li, X.; Feng, C.; Wang, R.; Liu, Y.; Yang, Y.; Yang, Y. Fuzzy Logic Control Based PID Controller for Diesel Engine with Variable Sampling Rate Control Theory. In Proceedings of the 2019 5th International Conference on Control Science and Systems Engineering (ICCSSE), Shanghai, China, 14–16 August 2019; pp. 84–87.
16. Yang, B. Genetic Algorithm–Optimized PID Control for Thermal Control Systems in Industrial Furnaces. *Int. J. Heat Technol.* **2025**, *43*, 2359. [CrossRef]
17. Kumar, V.; Rana, K. A novel fuzzy PID controller for nonlinear active suspension system with an electro-hydraulic actuator. *J. Braz. Soc. Mech. Sci. Eng.* **2023**, *45*, 189. [CrossRef]
18. Do, T.C.; Tran, D.T.; Dinh, T.Q.; Ahn, K.K. Tracking control for an electro-hydraulic rotary actuator using fractional order fuzzy PID controller. *Electronics* **2020**, *9*, 926. [CrossRef]
19. Yang, X.; Wu, D.; Wang, C.; Gao, C.; Gao, H.; Liu, Y. Adaptive fuzzy PID control of high-speed on-off valve for position control system used in water hydraulic manipulators. *Fusion Eng. Des.* **2024**, *203*, 114437. [CrossRef]
20. Wrat, G.; Bhola, M.; Ranjan, P.; Mishra, S.K.; Das, J. Energy saving and Fuzzy-PID position control of electro-hydraulic system by leakage compensation through proportional flow control valve. *ISA Trans.* **2020**, *101*, 269–280. [CrossRef] [PubMed]
21. Xu, C.; Xie, F.; Tian, Z.; Zhao, Z.; Chen, Z.; Li, Y. Fuzzy PID control strategy optimised by sparrow search algorithm for digital proportional valve with differential control of dual high-speed on/off valves. *Int. J. Hydromechatron.* **2025**, *8*, 444–467. [CrossRef]
22. Coskun, M.Y.; Itik, M. Intelligent PID control of an industrial electro-hydraulic system. *ISA Trans.* **2023**, *139*, 484–498. [CrossRef]
23. Jahedi, G.; Ardehali, M. Genetic algorithm-based fuzzy-PID control methodologies for enhancement of energy efficiency of a dynamic energy system. *Energy Convers. Manag.* **2011**, *52*, 725–732. [CrossRef]
24. Samakwong, T.; Assawinchaichote, W. PID controller design for electro-hydraulic servo valve system with genetic algorithm. *Procedia Comput. Sci.* **2016**, *86*, 91–94. [CrossRef]
25. Ye, Y.; Yin, C.B.; Gong, Y.; Zhou, J.J. Position control of nonlinear hydraulic system using an improved PSO based PID controller. *Mech. Syst. Signal Process.* **2017**, *83*, 241–259. [CrossRef]
26. Essa, M.E.S.M.; Aboelela, M.A.; Hassan, M.A.M. Position control of hydraulic servo system using proportional-integral-derivative controller tuned by some evolutionary techniques. *J. Vib. Control* **2016**, *22*, 2946–2957. [CrossRef]

27. dos Santos Coelho, L.; Cunha, M.A.B. Adaptive cascade control of a hydraulic actuator with an adaptive dead-zone compensation and optimization based on evolutionary algorithms. *Expert Syst. Appl.* **2011**, *38*, 12262–12269. [CrossRef]
28. Liu, Y.; Peng, X.; Chen, X.; Guo, Y. Electro-hydraulic proportional position control based on variable domain fuzzy PID. In Proceedings of the 2022 41st Chinese Control Conference (CCC), Hefei, China, 25–27 July 2022; pp. 2773–2778.
29. Cai, Y.; Zhao, Z.; Guo, W.; Xu, H.; Teng, Y.; Han, X.; Zhao, Q.; Wang, L. Smart Nutrient Solution Temperature Control System for Oversummering Lettuce Cultivation Based on Adaptive Dung Beetle Optimizer-Fuzzy PID. *Appl. Sci.* **2025**, *15*, 5381. [CrossRef]
30. Zhang, K.; As'arry, A.; Zhu, L.; Hairuddin, A.A.; Hassan, M.K.; Md Zain, M.Z. Enhancing ride comfort of semi-active suspension through collaboration control using dung beetle optimizer optimized Fuzzy PID controller. *Adv. Mech. Eng.* **2025**, *17*, 16878132251314332. [CrossRef]
31. Jelali, M.; Kroll, A. *Hydraulic Servo-Systems: Modelling, Identification and Control*; Springer Science & Business Media: Dordrecht, The Netherlands , 2012.
32. Xu, B.; Ding, R.; Zhang, J.; Su, Q. Modeling and dynamic characteristics analysis on a three-stage fast-response and large-flow directional valve. *Energy Convers. Manag.* **2014**, *79*, 187–199. [CrossRef]
33. Xue, J.; Shen, B. Dung beetle optimizer: A new meta-heuristic algorithm for global optimization. *J. Supercomput.* **2023**, *79*, 7305–7336. [CrossRef]
34. Kumar, A.; Price, K.V.; Mohamed, A.W.; Hadi, A.A.; Suganthan, P.N. *Problem Definitions and Evaluation Criteria for the CEC 2022 Special Session and Competition on Single Objective Bound Constrained Numerical Optimization*; Technical Report; Nanyang Technological University: Singapore, 2022.

Disclaimer/Publisher's Note: The statements, opinions and data contained in all publications are solely those of the individual author(s) and contributor(s) and not of MDPI and/or the editor(s). MDPI and/or the editor(s) disclaim responsibility for any injury to people or property resulting from any ideas, methods, instructions or products referred to in the content.